Journal of Materials Chemistry A

ROYAL SOCIETY OF CHEMISTRY

PAPER

View Article Online
View Journal | View Issue

Cite this: J. Mater. Chem. A, 2023, 11, 5910

Hierarchical flower-like MoS_2/reduced graphene oxide nanohybrids supported on nickel foam as a high-performance electrode material for supercapacitor applications†

Silki Sardana,[a] Sajjan Dahiya,[a] Rajesh Punia,[a] A. S. Maan,[a] Kuldeep Singh [b] and Anil Ohlan *[a]

The inconsistent characteristics of renewable energy sources have led to a continual imbalance between the need and supply of energy. Therefore, developing adequate energy-storage devices might be one solution to this ongoing issue. Supercapacitors are considered as predominant energy storage technologies and power sources to fulfil the energy demands of the modern lifestyle. The present article reports a simple one-pot hydrothermal route to prepare flower-like MoS_2/rGO (MG) nanohybrids followed by impregnation on nickel foam to develop the electrode for supercapacitors. The resultant MG-2 nanohybrid possessed a maximum specific capacitance of 2049.90 F g^{-1} at a current density of 30 mA g^{-1} and approximately 100% capacitive retention up to 10 000 successive charge–discharge cycles at 660 mA g^{-1}. Quantitative estimations were made to give detailed information on the contribution of the surface capacity and diffusion response to the overall charge-storage mechanism. In addition, a symmetric supercapacitor cell was designed using MG-2 nanohybrid electrodes, which achieved a high specific energy of 192.43 W h kg^{-1} and specific power of 337.36 W kg^{-1}. The remarkable electrochemical properties were attributed to the peculiar morphology of MG-2 nanohybrid having a distinctive 2D microstructure and minimal equivalent series resistance.

Received 28th October 2022
Accepted 14th February 2023

DOI: 10.1039/d2ta08416c

rsc.li/materials-a

1. Introduction

The demand for energy-storage systems with high power and energy density has been continuously increasing to fulfil the needs of modern lifestyles.[1] Supercapacitors are among the best energy-storage systems offering various enviable advantages, including high specific power, rapid charge–discharge characteristics, prolonged lifetimes, cost-effectiveness, and environmental benignity.[2] These unique features of supercapacitors open a portal for a myriad of applications in various industries, including hybrid electric vehicles, consumer electronics, memory backup devices, military equipment, and industrial power generation.[3] To date, substantial attempts have been devoted to make flexible and highly efficient supercapacitors using diverse carbon nanomaterials, metal oxides, conducting polymers, 2D materials and their composites.[4] Currently, 2D materials, such as graphene, TMDs, MOFs, MXenes, and LDHs, have attracted worldwide attention due to their outstanding features, which arise from their structure and dimensionality.[5] Transition metal dichalcogenides (TMDs), in particular, have been explored as an attractive alternative for the applications of supercapacitors because of their unique features.[3] Unlike graphene, which has a single carbon atom thick layer, TMDs possess a sandwich-like structure with a transition metal (Mo, Sn, Nb, V, W) layer integrated among two chalcogen (S, Se, Te) layers. TMDs exhibit strong covalent in-plane and weak non-covalent bonding between layers.[6] As a result, physical or chemical approaches, such as solvent-assisted exfoliation,[7] chemical exfoliation,[8] and adhesive tape exfoliation,[9] can be used to exfoliate bulk TMDs into solitary or few-layered structures. However, the outstanding properties of TMDs are offset by their possible agglomeration, which can hinder electrolyte ion transit and minimize the accessible surface area.[10] It is well-known that the incorporation of carbon-based materials with TMDs can modify the surface characteristics of 2D TMD nanosheets.[11] Considering all-carbon-based materials, graphene has received intensive interest for supercapacitor electrodes attributed to its outstanding features, which include a large specific surface area, flexible nature, high thermal and electrical conductivities, high mechanical strength, and rich chemistry.[12,13] Significant research on TMDs/carbon composite electrode-based supercapacitors has been reported and is still progressing.[14]

[a]Department of Physics, Maharshi Dayanand University, Rohtak-124001, India. E-mail: anilohlan@gmail.com; anilohlan.physics@mdurohtak.ac.in

[b]CSIR-Central Electrochemical Research Institute (CECRI) Chennai Unit, CSIR Madras Complex, Taramani, Chennai-600113, India

† Electronic supplementary information (ESI) available. See DOI: https://doi.org/10.1039/d2ta08416c

Among the TMDs, molybdenum disulfide (MoS_2) is considered as an auspicious supercapacitive material attributed to its higher capacitance, large specific surface area, outstanding cycle life, controllable band gap structure, and high catalytic activity.[15–17] Layered MoS_2 has drawn significant attention in diverse fields, such as electrochemical sensors,[18] energy-storage applications,[19] gas sensors,[20] photocatalysis,[21] photovoltaic cells,[22] and hydrogen-evolution reaction.[23] It can store charge *via* quick and reversible redox processes that vary the oxidation state of Mo in MoS_2 sheets.[24] The multiple oxidation states (+2 to +6) of the central Mo atom provide large pseudocapacitance.[25] Generally, MoS_2 possesses two crystal structures based on bonding and atomic stacking configurations: the octahedral (1T) phase and trigonal prismatic (2H) phase (the integer specifies the number of layers in the unit cell), as illustrated in Fig. 1. Each Mo atom in the 2H phase is linked prismatically to six adjacent S atoms producing a stable form, while six S atoms make a deformed octahedron around a single Mo atom in the metastable 1T phase.[26] Surprisingly, interlayer atomic gliding allows one phase to readily transition into the other phase. For example, the 2H phase can be transformed to the 1T phase by intercalating K or Li while the 1T phase progressively changes to the trigonal prismatic 2H phase because of its thermodynamic instability. 2H-MoS_2 is most commonly found in nature as a stable form with semiconductor characteristics, a large specific surface area, and a bandgap of 1.3–1.9 eV. However, 1T-MoS_2 has attracted significant interest in energy-storage applications, attributed to its higher electrical conductivity, hydrophilicity, and wider interlayer distance than 2H-MoS_2.[27] The 1T-MoS_2 phase is metastable during preparation, and is followed by development of the 2H phase, which degrades its conductivity to some extent. As a result, the benefits of both phases may be combined by creating mixed phases of MoS_2 using a one-step hydrothermal method.

If the thermodynamically stable 2H phase and highly conductive 1T phase are coupled in MoS_2 monolayers, then the properties of supercapacitor electrodes may be substantially improved.[28] Nanostructured MoS_2 has attracted immense interest for supercapacitors owing to its significant attributes[29] and such supercapacitors can be prepared using simple and cost-effective processes, like hydrothermal,[30,31] chemical vapour deposition,[32] liquid exfoliation,[33,34] chemical exfoliation,[35,36] and thermal evaporation–exfoliation[37] processes. For instance, Krishnamoorthy *et al.*[38] prepared a sphere-like MoS_2 nanostructure using a hydrothermal reaction, which possessed the highest specific capacitance of 92 F g^{-1} at 0.5 mA cm^{-2}. Thiourea was used both as a sulfur source and as a reducing agent. Nanostructured MoS_2 has been reported in various morphologies, including sheets, flowers, hollow spheres, rods, and many more.[39] Although many research papers have been published, research on highly efficient MoS_2-based supercapacitors is still ongoing to fulfil the demands for increasing energy.[40–42]

Herein, flower-like molybdenum disulfide/reduced graphene oxide (MG) nanohybrids were synthesized *via* a cost-effective and one-pot hydrothermal reaction. The resultant MG nanohybrids were successfully impregnated on nickel foam utilizing a dip-coating process and further employed for electrochemical characterizations. The mass loading of the active material was estimated using the weight differential of nickel foam after and before coating.

2. Experimental section

2.1. Reagents

Sodium molybdate dihydrate ($Na_2MoO_4 \cdot 2H_2O$), potassium permanganate ($KMnO_4$), sulfuric acid (H_2SO_4) and thiourea (CH_4N_2S) were purchased from Merck. Natural graphite flakes and *N*-methyl-2-pyrrolidone (NMP), were procured from Himedia and hydrogen peroxide (H_2O_2) from Sigma Aldrich. Conducting carbon black and poly (vinylidene fluoride) (PVDF) were purchased from Alfa Aesar. High-grade nickel foam with 1.5 mm thickness, purity of >99%, and porosity of 95–98% was

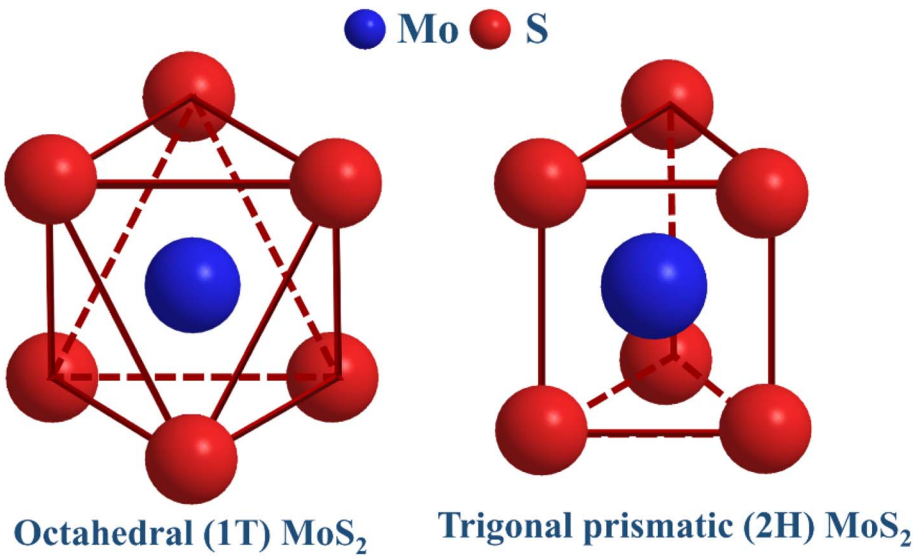

Fig. 1 1T and 2H phases of MoS_2.

purchased from Vritra Technology, India. Distilled water was utilized in all the experiments to assure the sample quality and avoid external contamination.

2.2. Synthesis of molybdenum disulfide (MS)

In a typical synthesis, 2.0 mmol $Na_2MoO_4 \cdot 2H_2O$ and 8.0 mmol CH_4N_2S were homogeneously dispersed in distilled water and stirred at an appropriate speed for 1 h. This mixture was poured in a 200 mL Teflon-lined autoclave for hydrothermal reaction at 200 °C for 24 h. Upon completion of the reaction, the autoclave was brought to normal temperature. The resultant MoS_2 precipitates were repeatedly rinsed with distilled water until the final product was entirely free of remnant ions. After that, the resulting precipitates were dried overnight at 80 °C. A schematic elucidation of the preparation of flower-like MoS_2 nanosheets *via* a hydrothermal reaction is presented in Fig. 2.

2.3. Synthesis of MoS_2/rGO (MG) nanohybrids

Prior to the formation of MoS_2/rGO (MG) nanohybrids, graphene oxide was synthesized using a modified Hummer's method.[43] In brief, graphite flakes (5 g) were expanded 100–150 times to their initial volume in a microwave oven for 10 s and then dissolved in conc. H_2SO_4 (1000 mL) in an ice bath while stirring continuously. Afterward, $KMnO_4$ (20 g) was added gently, keeping the temperature below 20 °C to avoid explosion. The suspension was vigorously stirred for 2 h at ambient temperature. The solution was chilled in an ice bath and gradually diluted with ice water keeping the temperature below 70 °C. Also, 50 mL of H_2O_2 (30 wt%) was added to ensure that the reaction was completed with $KMnO_4$. The resultant suspension was centrifuged, and rinsed with 10% HCl solution and distilled water multiple times to remove the acid until its pH value reached neutral. Finally, the graphene oxide (GO) was collected after filtration and dehydrated at 60 °C for 48 h.

For synthesizing MG nanohybrids, a certain amount of GO dispersion was added into a solution containing 2.0 mmol $Na_2MoO_4 \cdot 2H_2O$ and 8.0 mmol CH_4N_2S. Different samples were synthesized by changing the amount of GO (0.5, 1, 2 g mL^{-1}), keeping the same amount of other reactants, and were denoted as MG-0.5, MG-1, and MG-2, respectively. The synthesis protocol was similar to that of pure MoS_2 and is schematically displayed in Fig. 3.

2.4. Fabrication of the electrodes and supercapacitor cell

The supercapacitor electrodes were prepared by dispersing the active material, binder PVDF, and conducting carbon black in NMP solution in a weight ratio of 85 : 5 : 10, respectively. Nickel foam was invoked as a substrate for depositing the as-synthesized samples. The slurry was uniformly coated on nickel foam by a simple repetitive dip-coating technique. Subsequently, the MG nanohybrid-impregnated Ni foam was dried at 60 °C for few hours in an oven to ensure an adequate evaporation of the solvent NMP. The electrochemical measurements were performed in a Swagelok Teflon cell assembly, which included two symmetrical electrodes of the MG nanohybrid, filter paper as the separator, and 1 M Na_2SO_4 aqueous solution as the electrolyte. The mass loading of active material was 6 mg cm^{-2}. Before assembling the supercapacitor cell, the electrodes were submerged in 1 M Na_2SO_4 solution for few hours to ensure that the electrolyte was evenly distributed throughout the electrodes.

3. Results and discussion

The flower-like MoS_2 microspheres comprised of nanosheets were synthesized *via* a one-pot hydrothermal approach employing thiourea as the sulfur source and sodium molybdate as the molybdenum source. The formation of the hierarchical flower-like morphology was a "three-step growth" mechanism involving the fast synthesis of amorphous primary particles, aligned nanosheets aggregation, and the self-assembly of the hierarchical structure.[44] The chemical reaction that occurred during the hydrothermal process is shown in Fig. 2.

During the hydrothermal reaction, sodium molybdate produced MoO_4^{2-} and NH_4^+, while thiourea provided sulfur. In this reaction, thiourea reduced MoO_4^{2-} to MoS_2 and GO to rGO at the same time. Thus, MoS_2 was formed when MoO_4^{2-} interacted with the sulfur ions, and the residual ammonia intercalation prevented the MoS_2 nanostructures from stacking, resulting in their self-assembly into a sphere-like shape. The hydrothermal reaction conditions and the role of precursors promoted the formation of porous MoS_2 nanostructures that

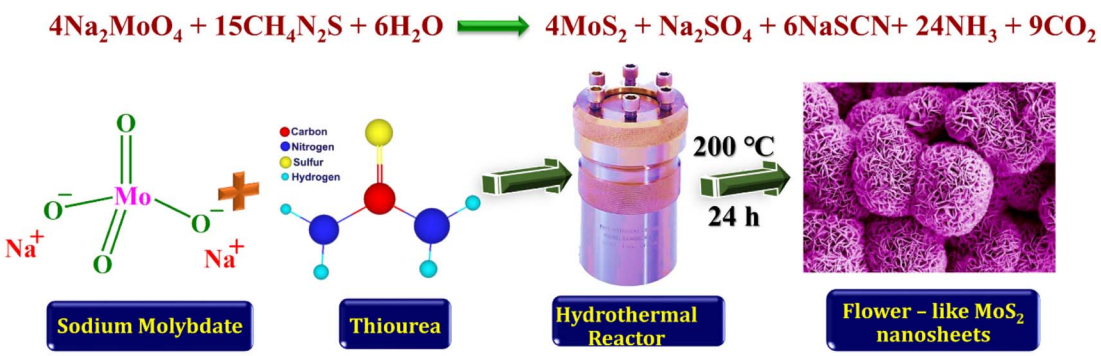

Fig. 2 Schematic representation for synthesizing flower-like MoS_2 nanosheets *via* hydrothermal reaction.

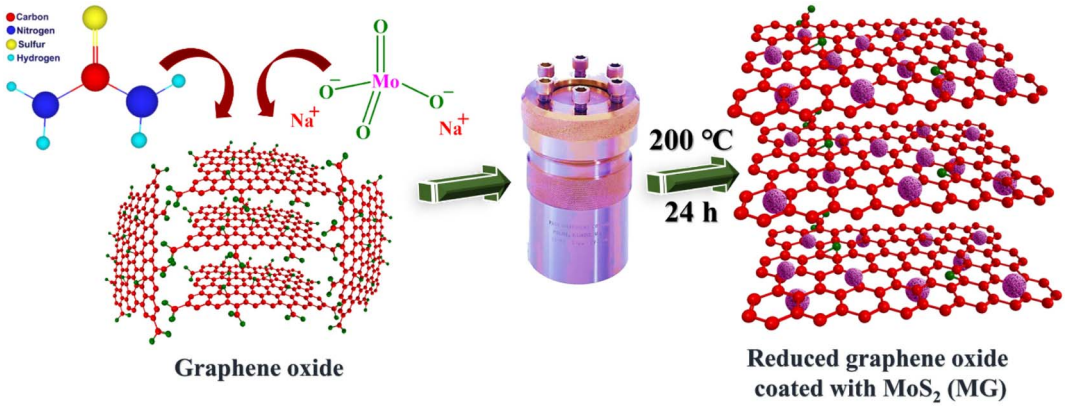

Fig. 3 Schematic for the synthesis of MG nanohybrids *via* hydrothermal reaction.

were joined together into a spherical shape. The rGO network aided in disseminating the MoS_2 nanosheets and provided a conductive path between the active interface centre and the current collector, while the surface area of MoS_2 mitigated the ion-diffusion length and gave an upsurge in the ion-diffusion rate. The flower-shaped MoS_2 were uniformly decorated onto rGO nanosheets *via* their oxygen-containing functional groups. Thus, the as-synthesized three-dimensional architecture of MG nanohybrids facilitated better electrode–electrolyte interactions, which improves supercapacitor performance.

3.1. XRD analysis

Fig. 4(a) presents the XRD patterns of MS and MG nanohybrids. The positions of the peaks and their corresponding planes were indexed. The XRD spectra of MS showed five diffraction peaks at $2\theta = 14.0°$, 32.5°, 35.8°, 42.9°, and 57.4°, corresponding to the (002), (100), (103), (105), and (110) planes, respectively, as per the reported values for the layered morphology (JCPDS no. 65-1951). The solitary peak centred at $2\theta = 14.0°$ could be attributed to the presence of crystallinity in the sample. Furthermore, the XRD pattern showed no extra peaks of any contaminants, implying that the resultant MS was of high purity. In addition, all the MG nanohybrids showed a peak around 24.9°, corresponding to the (002) reflection of the graphitic carbon of rGO. It could be seen that as the concentration of GO increased in the MG nanohybrid, the peak corresponding to rGO became more pronounced.

3.2. Raman spectra

Raman spectra were recorded to analyze MS and MG nanohybrids, as it is particularly sensitive for analyzing microstructure materials. Fig. 4(b) displays the Raman spectra of MS and MG nanohybrids collected at 532 nm excitation wavelength. The distinct phonon modes at 148.9 (J_1), 196.2 (J_2), and 336.2 cm^{-1} (J_3) were characteristic of the metallic 1T phase. The presence of the 2H phase was indicated by the distinctive peak positions at 447.9, 401.5, and 376.4 cm^{-1}, corresponding to the second-order Raman scattering 2LA(M), out-of-plane Mo–S vibration mode (A_{1g}), and in-plane Mo–S mode (E2g1), respectively.[45] The in-plane E^1_{2g} mode was caused by two S atoms vibrating in different directions about the Mo atom, whereas the out-of-plane A_{1g} mode was induced by just two S atoms vibrating in opposite directions.[46] It was also observed that the A_{1g} peak had a substantially higher intensity than E^1_{2g}, suggesting that the as-synthesized MoS_2 possessed a rich edge-terminated structure. The presence of all these Raman peaks confirmed the mixed 1T/

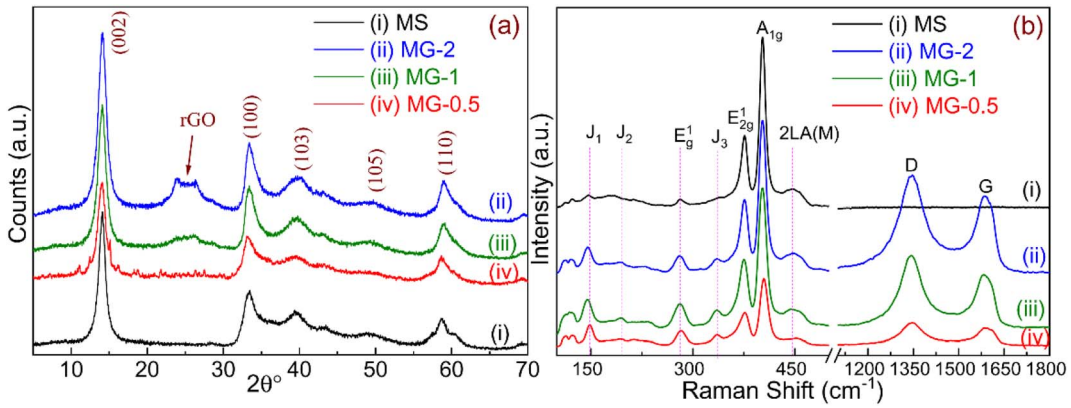

Fig. 4 (a) XRD and (b) Raman spectra of MS, MG-0.5, MG-1, and MG-2 nanohybrids, respectively.

2H-MS phase. The characteristics of the 1T/2H phases of MS were credited with the good electrochemical performance. Furthermore, two pronounced peaks were observed at 1583 and 1345 cm^{-1} in all the MG nanohybrids, corresponding to the G and D bands of rGO, respectively, confirming the reduction of GO to rGO. This finding confirmed the formation of mixed-phase MS and the presence of rGO in MG nanohybrids.

3.3. Morphological analysis

The morphological evolutions of pristine MS and MG nanohybrids were ascertained using FESEM micrographs, as displayed in Fig. 5. Fig. 5(a and b) present the FESEM micrographs of pristine MS at different magnifications, and it could be observed that MS possessed a symmetrical flower-like morphology. Many irregular MS nanosheets aggregated to form nanoflowers, illustrating that the resultant MS contained a porous structure.

The FESEM image of MG-2 shows that the accumulation of MS nanoflowers had been suppressed and distributed on rGO nanosheets during the *in situ* hydrothermal reaction. After graphene was incorporated into the solution, the sheet-like subunits united to form a three-dimensional nanostructure. Fig. 5(c and d) depict that the MS nanosheets were uniformly distributed on rGO nanosheets, creating a hierarchical 3D network framework and influencing the accomplishment of a high charge-storage capability. The MG nanosheets were joined together by van der Waals interactions and then self-assembled into three-dimensional nanostructures. The incorporation of MS into rGO nanosheets restricted the agglomeration of rGO layers to some extent, which would yield additional active sites for ion intercalation and deintercalation.

Fig. 6(a–c) show the high-magnification FESEM images of Ni-foam-coated MG-0.5, MG-1, and MG-2 nanohybrids, respectively, while the corresponding FESEM images at lower magnification are shown in Fig. S1.† The high-magnification FESEM images of the Ni-foam-coated MG nanohybrids showed hierarchical 3D porous and interconnected structures in which MoS_2 nanosheets incorporated with rGO layers were well-coated onto/within the pores of Ni foam. The images show that the MG nanohybrids and Ni foam adhered well upon dip-coating due to the weak van der Waals interaction between Ni foam and MG nanohybrid. Furthermore, the high conductivity and porous structure of Ni foam provide an effective conductive channel for the movement of electrons/ions during redox reactions.[38] Next, EDX elemental mapping was carried out for the as-prepared MG-2 nanohybrid to further analyze the dispersion of the constituent elements (Fig. 6(d–g)). The atomic composition of the constituent elements C, O, S, and Mo of MG-2 nanohybrid observed by semi-quantitative EDX spectrum analysis is displayed in Fig. 6(h). The elemental mapping of MG-2 nanohybrid exhibited a homogeneous distribution of the elements C, O, Mo, and S (Fig. 6(i)). This further demonstrates that MS nanospheres were evenly dispersed throughout the rGO matrix.

Transmission electron microscopy (TEM) was used to further describe the intriguing structure of the MG nanohybrid. Fig. 7(a

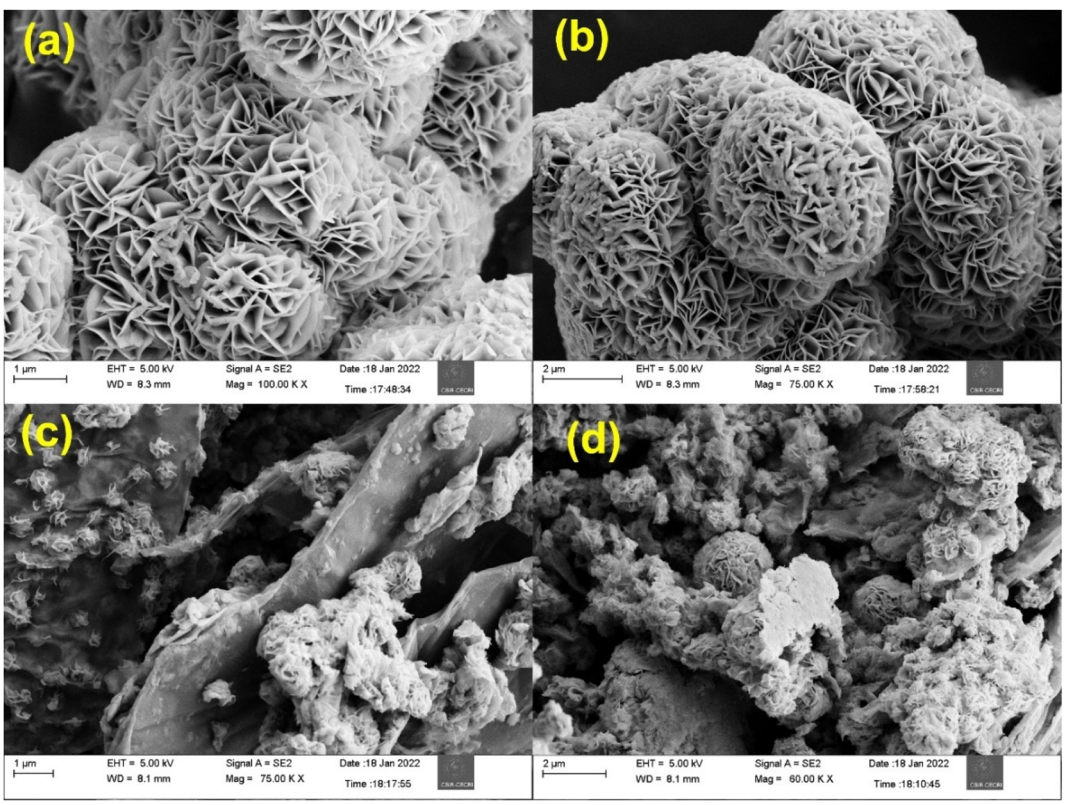

Fig. 5 FESEM images of (a, b) MS and (c, d) MG-2 at different resolutions, respectively.

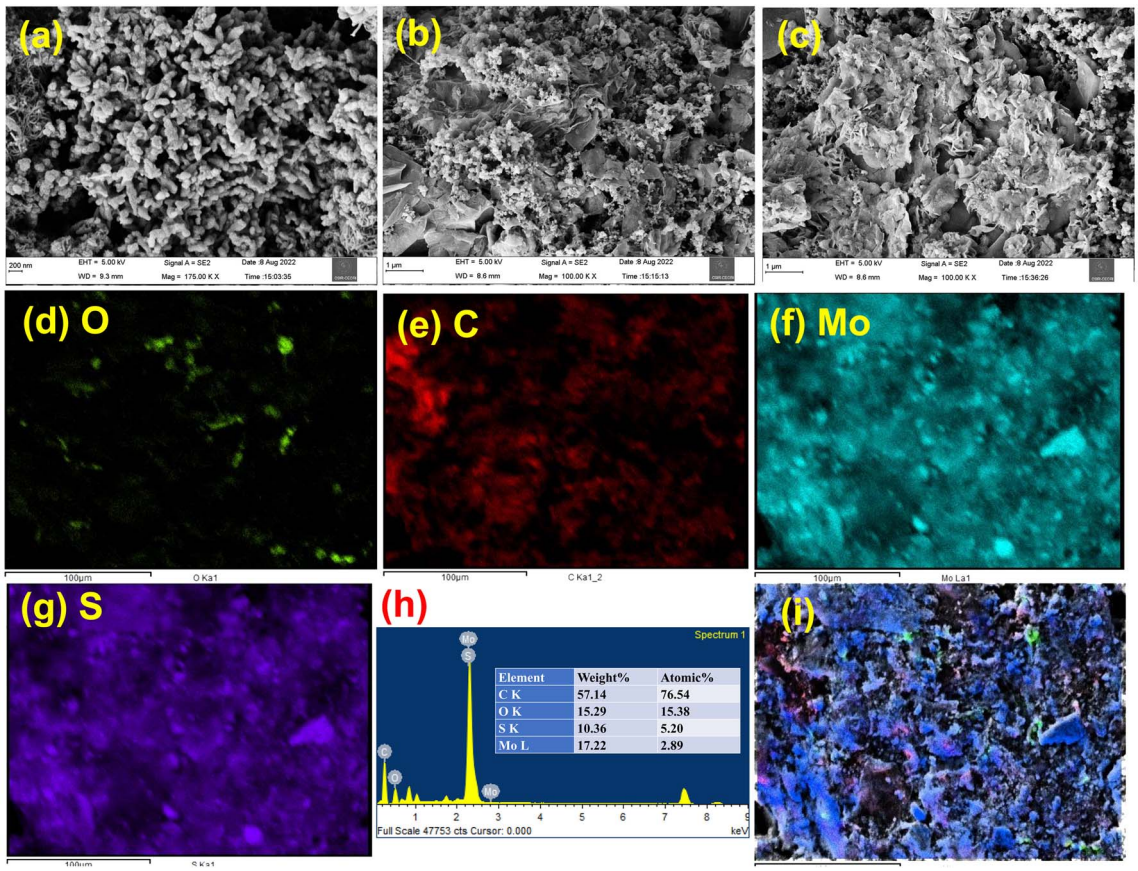

Fig. 6 High-magnification FESEM images of Ni-foam-coated (a) MG-0.5, (b) MG-1, and (c) MG-2; EDX elemental mapping of (d) O, (e) C, (f) Mo, and (g) S; (h) atomic composition of the constituent elements C, O, S, and Mo of MG-2; and (i) EDX elemental mapping of MG-2 nanohybrid.

and b) show the TEM images of MG-2 nanohybrid at different resolutions, showing the crumpled layered structure of rGO nanosheets decorated by MoS_2 nanoflowers. The crumpled layered structure of rGO showed a wrinkled and rough texture. In addition, atomic-scale images of MG-2 nanohybrid were obtained by high-resolution scanning transmission electron microscopy equipped with a high angular annular dark-field detector (HR STEM-HAADF). Fig. 7(c and d) present the HRTEM images of MG-2 nanohybrid illustrating the interlayer lattice fringes of 0.65 nm. The HR STEM image clearly showed a few layers of graphene nanosheets that were vertically aligned. The contrast pattern of MG-2 nanohybrid mimicked the structure of the MS lattice with its (001) basal plane parallel to the surface of rGO. The STEM HAADF image of MG-2 nanohybrid is shown in Fig. 7(e). Fig. 7(f–i) display the HAADF images, illustrating the elemental composition of MG-2 nanohybrid, thus confirming the presence of the constituent elements.

3.4. N_2 adsorption–desorption isotherms

The porous structure and specific surface area of MS and MG-2 nanohybrid were investigated using N_2 adsorption–desorption isotherms. Fig. 8(a) shows isotherms of MS and MG-2 nanohybrid. According to IUPAC classification, the N_2 isotherms of both samples revealed a type-IV isotherm and H3 hysteresis loops, reflecting a mesoporous structure. These 3D mesopores are effective for energy-storage applications, as they can serve as "reservoirs" for the electrolyte to shorten the diffusion length. The MS and MG-2 nanohybrid possessed Brunauer–Emmet–Teller (BET) specific surface areas of 3.882 and 7.74 $m^2\ g^{-1}$, respectively. The specific surface area of MG-2 nanohybrid had been increased by the incorporation of rGO.

Fig. 8(b) shows the pore-size distribution, in which mesopores with an average diameter of 8.82 nm and pore volume of 0.082 $cm^3\ g^{-1}$ were observed for MG-2 nanohybrid, while MS possessed an average pore diameter of 6.06 nm and pore volume of 0.026 $cm^3\ g^{-1}$. The mesoporous nature of the nanostructure with pore diameters ranging from 2–50 nm facilitates fast electrolyte diffusion and mass transportation, resulting in a better capacitive performance. A hierarchical porous structure was also evident in the size distribution of the pores, with the majority being mesopores and with some micropores and macropores sprinkled throughout. Such intriguing features of MG-2 nanohybrid make it beneficial for transport and ion diffusion at the time of charging/discharging, thus resulting in better electrochemical performance. Fig. 8(c) displays the increment in the adsorbed volume with the increase in layer thickness. The increase in thickness of the layers deposited with increasing relative pressure (P/P_o) is presented in Fig. 8(d).

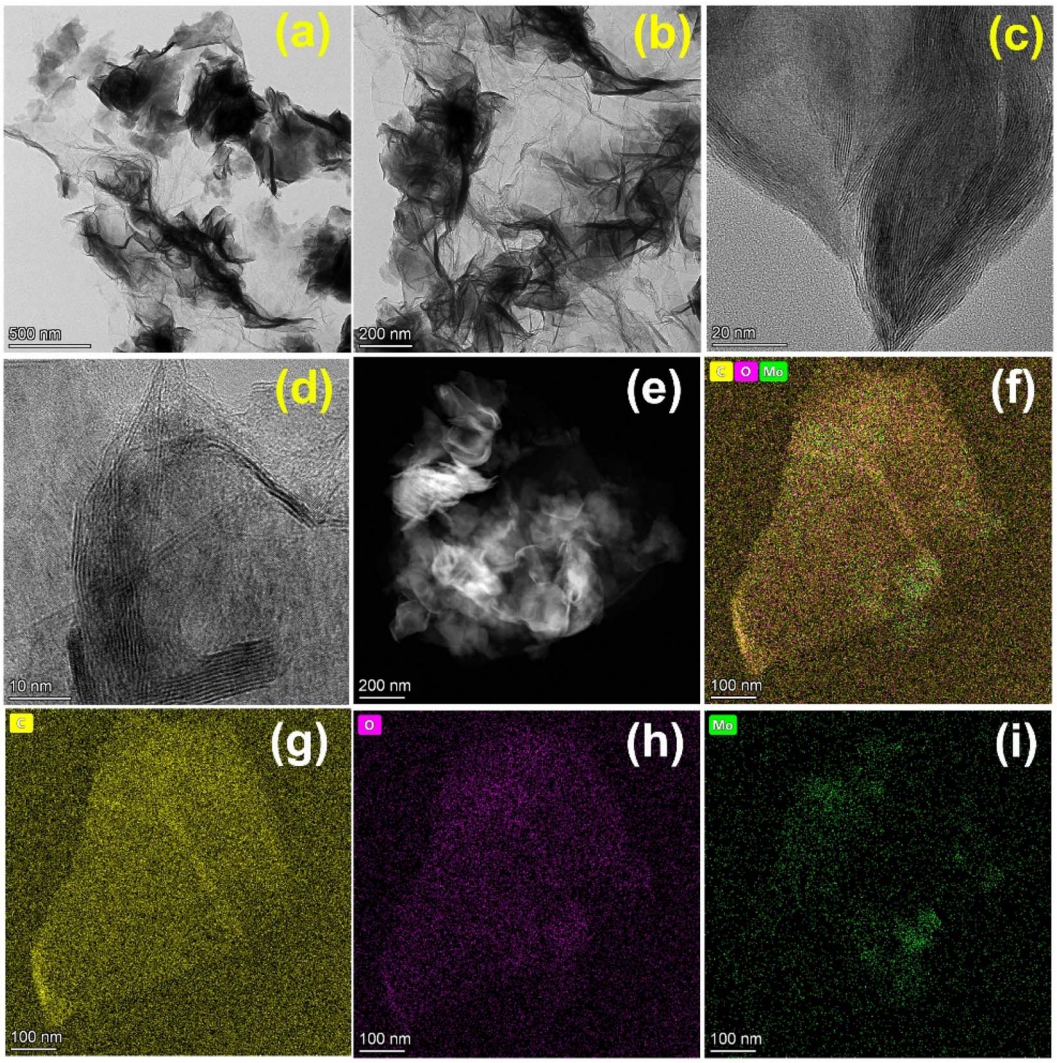

Fig. 7 (a) and (b) TEM images at different resolutions, (c) and (d) HRTEM images showing the lattice fringes, (e) HR STEM image, (f)–(i) HAADF images showing the elemental composition of the MG-2 nanohybrid, respectively.

3.5. XPS analysis

XPS was used to assess the structural characteristics and elemental composition of the as-synthesized samples. Fig. 9(a) depicts the XPS survey spectrum of MG-2 nanohybrid, in which the presence of the predominant elements Mo, S, O, and C could be distinctly observed. The primary constituents of the as-synthesised MG-2 were validated by the peaks in the XPS spectrum indexed to Mo 3d, S 2p, O 1s, N 1s, and C 1s. Fig. 9(b–e) display the high-resolution XPS scans of MG-2 for the Mo 3d, C 1s, S 2p, and O 1s regions, respectively. The high-resolution XPS data for Mo 3d/S 2s were deconvoluted into multiple peaks: two strong peaks of 1T-Mo $3d_{5/2}$ (227.3 eV) and 1T-Mo $3d_{3/2}$ (230.5 eV), suggesting the Mo(IV) oxidation state of MS. Besides, two relatively weak peaks of 2H-Mo $3d_{5/2}$ (229.3 eV) and 2H-Mo $3d_{3/2}$ (233.2 eV) were observed, showing the Mo(VI) oxidation state of MS.

The weak peak located at 224.5 eV corresponded to S 2s. The deconvoluted S 2p scan showed two strong peaks at 160.1 and 161.4 eV, which were attributed to 1T-S $2p_{3/2}$ and 1T-S $2p_{1/2}$, respectively. Besides, two weak peaks also appeared at 160.9 and 167.2 eV for 2H-S $2p_{3/2}$ and 2H-S $2p_{1/2}$, respectively. The peaks at 286.4, 284, and 282.6 eV in the C 1s scan could be attributed to C–O, COOH/C=O, and C=C/C–C, respectively, confirming the reduction of GO into rGO. In the fitted O 1s spectra, the peaks at 528.5, 530.7, and 531.9 eV were ascribed to C=O, C–O, and C–OH groups, correspondingly. Furthermore, the atomic percentages were calculated directly from the XPS study, as illustrated in Fig. 9(f). The appearance of both 1T/2H phases will result in better electrochemical performance.

3.6. Electrochemical measurements

Fig. 10(a) illustrates the qualitative comparison between the CV plots of pure MS and MG nanohybrids at a scan rate of 1 mV s^{-1}. All the CV plots differed from the ideal rectangular curve emanating from a pure EDLC behaviour, indicating the characteristics of pseudocapacitance. It was seen that the current

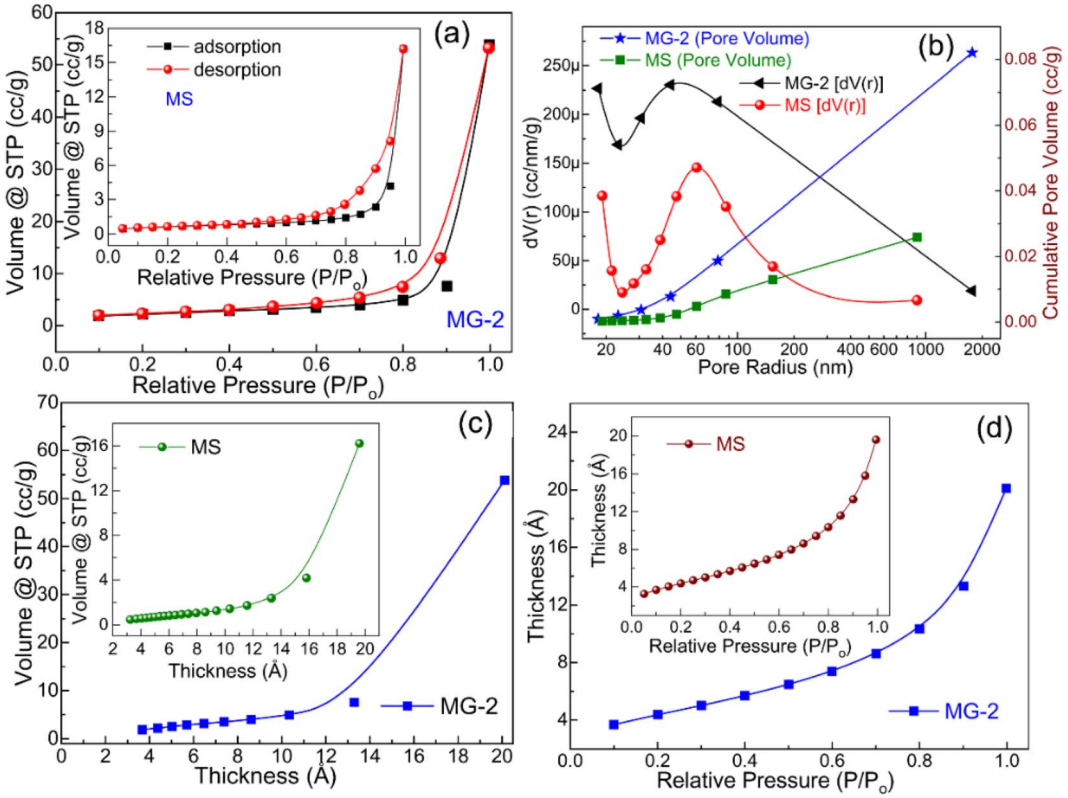

Fig. 8 (a) N_2 isotherm curves, (b) pore-size distribution, (c) volume of N_2 adsorbed with the deposited layers thickness, and (d) change in the deposited layers thickness with the P/P_o of MS and MG-2 nanohybrid.

increased through the inclusion of rGO in MS. This might be ascribed to the high electrical conductivity and optimum utilization of active sites of MS after the incorporation on rGO. Fig. 10(b) displays the CV curves at different scan rates (0.2–5 mV s^{-1}) for further investigation of the MG-2 nanohybrid features. The area under the CV plot increased accordingly with the scan rate (0.2–5 mV s^{-1}), indicating the fast kinetics of interfacial redox reactions and ion/electron transmission. Furthermore, the oxidation and reduction peaks were symmetrical and slightly displaced, showing that the faradaic redox reaction occurring at the electrode surface was quasi-reversible. The complex and intermediate behaviour of MG-2 nanohybrid was ascribed to the synergetic effect of surface capacitive processes (EDLC and surface redox reactions) and diffusion-regulated processes, most likely caused by the diffusion and intercalation/deintercalation of electrolyte ions in the interlayer spacing of the 2D nanohybrid.

The following equation was implemented to evaluate the specific capacitance of MG nanohybrid:

$$C_s = \frac{1}{m \times v \times V} \int I(V)\mathrm{d}V \quad (1)$$

where m, v, V, and $\int I(V)\mathrm{d}V$ are the mass of active material, scan rate, operating voltage, and area enclosed under the CV curve, respectively.

The value of C_s for MG-2 nanohybrid was calculated as 1397.85 F g^{-1} at a scan rate of 0.2 mV s^{-1}. The high value of C_s was credited to the contribution of MS having an excellent electrochemical activity that provides pseudocapacitance *via* faradaic reactions in which electrolyte ions diffuse into the MS layer as well as electric double-layer capacitance (EDLC) *via* a non-faradaic reaction with charge accumulation at the electrode–electrolyte interface. The value of C_s dropped with increasing the scan rate, which was attributed to the sluggish movement and prolonged intercalation time of ions of the electrolyte in the active material.[47] In addition, the faradaic process in MG-2 may be ascribed to the phase transformation from 2H to 1T and *vice versa* for MoS_2 during the charging and discharging process, respectively, in neutral Na_2SO_4 electrolyte. Upon charging, Na^+ ions inserted in to the MoS_2 interlayers and while discharging, they get extracted from the layers, leading to the reversible redox processes.[48] Fig. 10(c) shows the declination in C_s with the scan rate. Moreover, the shape of the CV plot was practically consistent even at higher scan rates, demonstrating that MG-2 possessed a reasonable rate and capacitive performance.

To better understand the charge-storage processes in MG-2 nanohybrid electrodes, the Trassati plot was utilized.[49] A Trasatti plot separates the capacitance contributions from EDLC and pseudocapacitive processes. The total capacitance (C_T) can be determined using the Trasatti method by estimating the capacitance at $v = 0$ from $1/C$ *vs.* $v^{1/2}$ plot (Fig. 11(b)). On the other hand, electric double-layer capacitance (C_o) was calculated at $v = \infty$ from the C *vs.* $v^{-1/2}$ plot (Fig. 11(a)). The

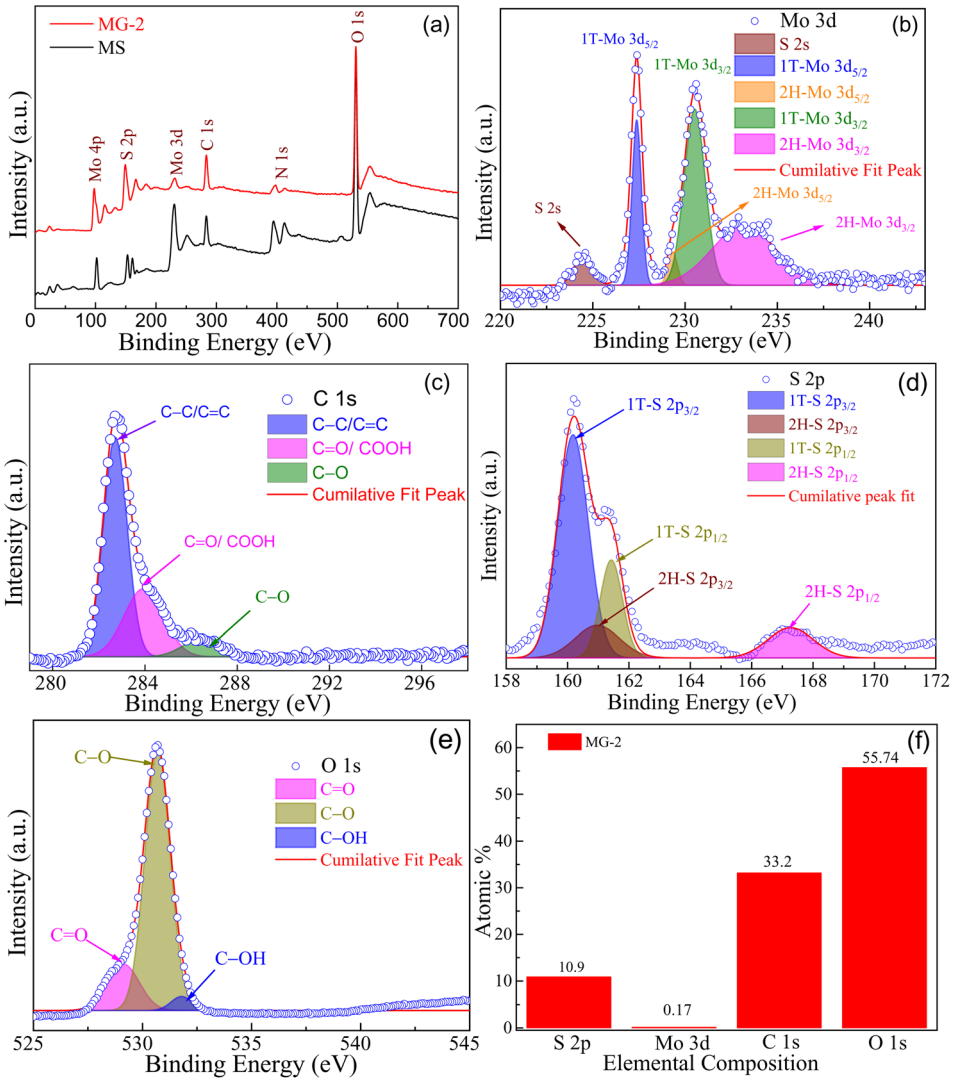

Fig. 9 (a) XPS survey spectra of MS and MG-2 nanohybrid; high-resolution XPS of (b) Mo 3d/S 2s scan, (c) C 1s scan, (d) S 2p scan, and (e) O 1s scan; and (f) corresponding elemental composition of MG-2 nanohybrid.

difference between C_T and C_o can be used to find the pseudocapacitive contribution.[50] Fig. 11(c) shows a histogram showing the capacitance contribution from EDLC and pseudocapacitance. It was observed that the EDLC contributed 63% to the total capacitance.

The charge-storage capability of the MG-2 nanohybrid electrode was semi-quantitatively resolved by analyzing the current response of the CV curve at varying scan rates. The current (I) and scan rate (v) follow the power law:

$$I = av^b \quad (2)$$

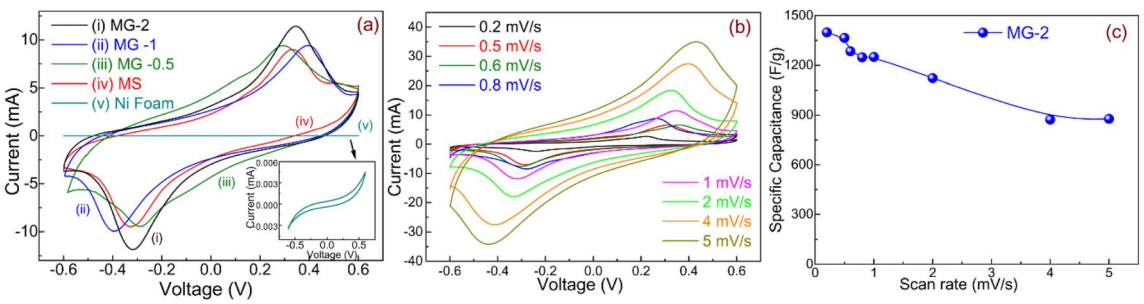

Fig. 10 (a) CV plots of MS, MG-0.5, MG-1, and MG-2 nanohybrids; (b) CV curves of MG-2 at several scan rates (0.2–5 mV s^{-1}); and (c) variation in specific capacitance of MG-2 with the scan rate.

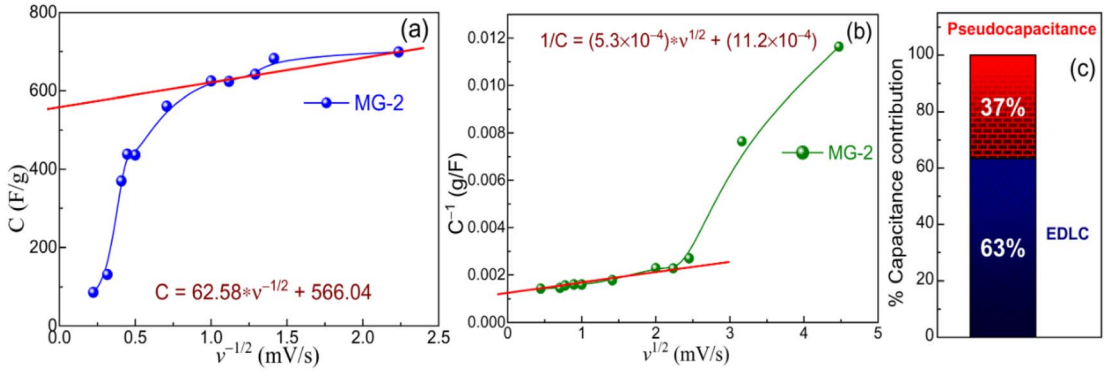

Fig. 11 Trasatti method: (a) plot of C with $v^{-1/2}$, (b) plot of $1/C$ with $v^{1/2}$, and (c) histogram showing the capacitance contribution from EDLC and pseudocapacitance.

where a and b are adjustment constants. The b-value was calculated for the positive and negative scans, from the slope of $\log(I)$ and $\log(v)$ graph. For $b = 0.5$, charge storage is regulated by a semi-infinite diffusion mechanism ($I \propto v^{1/2}$) but if $b = 1$, charge storage is governed by the surface capacitive process ($I \propto v$). The variations of the cathodic and anodic peak currents with the scan rate for MG-2 nanohybrid are depicted in Fig. 12.

Considering the positive and negative scans, the b-values lay between 0.5 and 1, suggesting that the current was dominated by capacitive behaviour. Thus, the total charge-storage behaviour was regulated by capacitive- and diffusive-controlled mechanisms. The current response at a certain potential can be represented as the addition of capacitive and diffusion processes:[51]

$$I(V) = k_1 v + k_2 v^{1/2} \quad (3)$$

For quantitative purposes, we divide both sides of eqn (3) by $v^{1/2}$, and get:

$$\frac{I(V)}{(v)^{1/2}} = k_1 (v)^{1/2} + k_2 \quad (4)$$

where $I(V)$ denotes the current at a given voltage, k_1 and k_2 are the scan rate-independent parameters, v is the scan rate, $k_1 v$ stands for the current produced by surface-controlled capacitive processes (combination of EDLC and rapid redox reactions), and $k_2 v^{1/2}$ stands for the current generated by diffusion-controlled or sluggish kinetics. The values of k_1 and k_2 were estimated from the slope and intercept of the graph of $I(V)/v^{1/2}$ and $v^{1/2}$. Therefore, the contribution of capacitive and diffusion current could be differentiated as shown in Fig. 13. It could be seen that raising the scan rate resulted in a drop in the % contribution from the diffusion current. The capacitive contributions were 70%, 72%, 76%, 79%, 78%, and 87% of the total capacitance for the scan rate varying from 0.2 to 2 mV s^{-1}, respectively. The shaded areas show the capacitive contribution and the histogram shows the capacitance contributions of capacitive and diffusive processes at different scan rates for MG-2 nanohybrid.

The comparative GCD curves of pristine MS and MG nanohybrids at a current density of 150 mA g^{-1} are displayed in Fig. 14(a). It can be seen that all the GCD curves showed a slight deviation from perfect linearity, indicating the pseudocapacitive behaviour of the electrode material. Using the GCD data, the essential parameters of supercapacitor devices, including specific capacitance (C_s), specific energy (E_s), and specific power (P_s), can be measured using the following equations:

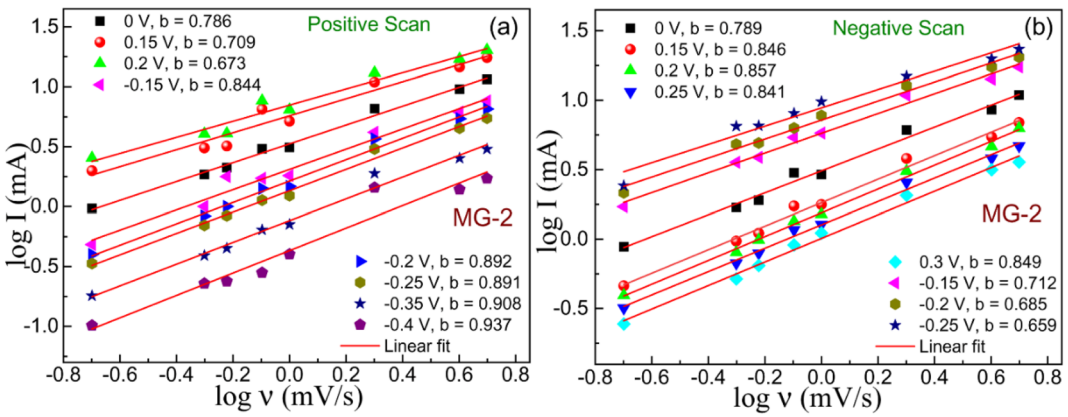

Fig. 12 Variations of the cathodic and anodic currents with the scan rate for MG-2 nanohybrid.

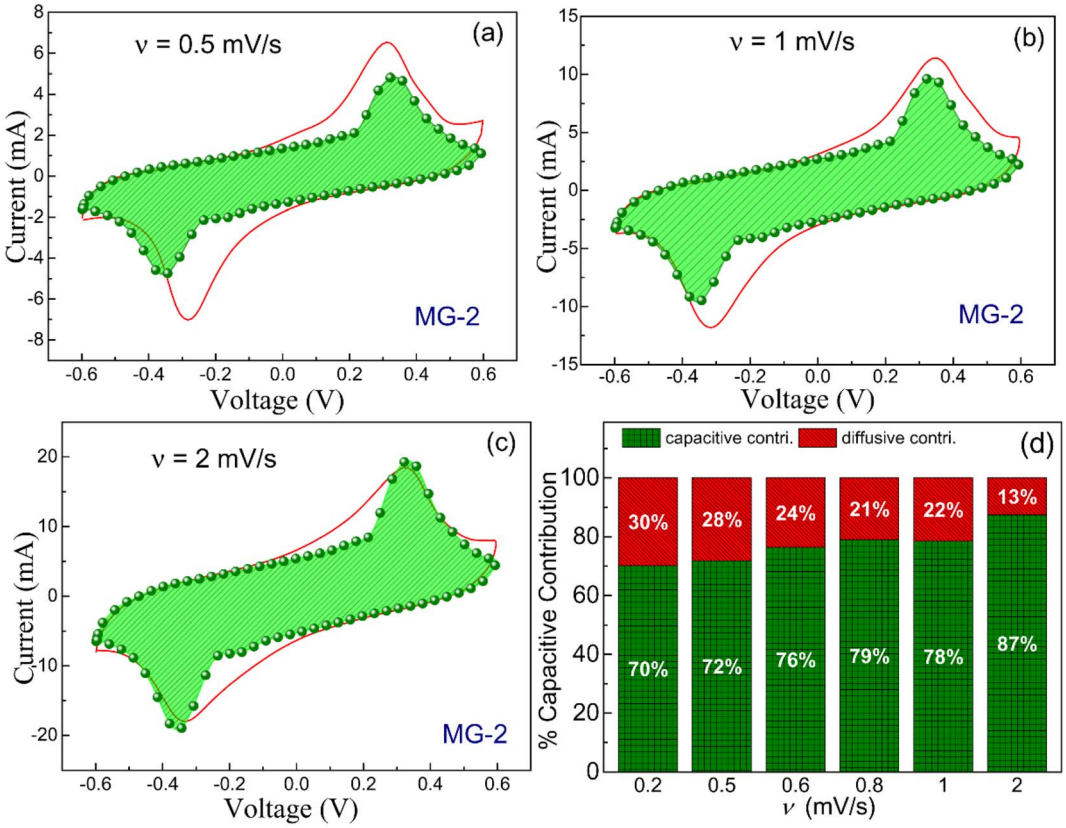

Fig. 13 Dunn method analysis of the capacitance contribution for (a) $v = 0.5$, (b) $v = 1$, (c) $v = 2$ mV s^{-1}, and (d) histogram showing the capacitance contributions of capacitive and diffusive processes at different scan rates for MG-2 nanohybrid.

$$C_s = \frac{I \times t_d}{m \times \Delta V} \quad (5)$$

$$E_s = \frac{C_{cell}(\Delta V)^2}{2M} \times \frac{10}{36} \quad (6)$$

$$P_s = \frac{(\Delta V)^2}{4M\ \mathrm{ESR}} \times 1000 \quad (7)$$

where I, ΔV, m, t_d, C_{cell}, and ESR are the current, voltage window, mass of active material, discharging time, cell capacitance, and equivalent series resistance, respectively.

The rate capability is also a significant parameter for energy-storage applications. Therefore, GCD data were collected for MG-2 nanohybrid at a variety of current densities (30–150 mA g^{-1}), as illustrated in Fig. 14(b). The value of C_s for MG-2 nanohybrid was evaluated to be 2049.90 F g^{-1} at a current density of 30 mA g^{-1}, which remained as 1032.98 F g^{-1} at 150 mA g^{-1}, suggesting the outstanding rate capability of the material. Fig. 14(c) shows the variation in C_s of MG-2 nanohybrid with increasing the current density. At current densities ranging from 30–150 mA g^{-1}, the GCD curves displayed almost linear and symmetric behaviour, implying high reversibility of the electrode material. Table 1 shows the values of C_s calculated using CV and GCD data. The cycle stability of MG-2 nanohybrid was evaluated using GCD measurements. As shown in Fig. 14(d), after cycling for 10 000 successive cycles at a fixed current density of 660 mA g^{-1}, the C_s retained approx. 100% of its original value. It was quite interesting to note that the capacitance retention increased initially for 2000 cycles due to the activation of rGO.[52] The cyclic performance demonstrate that the as-synthesized electrode material possessed superior cyclic stability, which is comparable with already published TMD-based supercapacitors.[53,54] In addition, the as-fabricated MG-2-based supercapacitor device exhibited a maximum E_s of 192.43 W h kg^{-1} and P_s of 337.36 W kg^{-1} at 30 mA g^{-1} and delivered an E_s of 81.63 W h kg^{-1} and P_s of 330.83 W kg^{-1} at 150 mA g^{-1}. The schematic design of the supercapacitor electrode assembly is presented in Fig. 15.

EIS analysis is used to assess the electrochemical reaction kinetics of electrode materials. Fig. 16(a) presents Nyquist plots for MS and MG nanohybrids. At high frequencies of the Nyquist plot, the intercept with the real axis reflects R_s, which often comprises the inherent resistance of the electrode, electrolyte, and interfacial resistance between Ni foam and the active material.[55] The diameter of the semicircle represents the charge-transfer resistance (R_{ct}), which is caused by EDLC and redox processes at the electrolyte/electrode intersection. In the low-frequency part, a nearly vertical line indicates diffusion of ions at the electrolyte/electrode intersection. The presence of Warburg impedance or diffusion resistance, represented by W, is responsible for the divergence from a perfect vertical

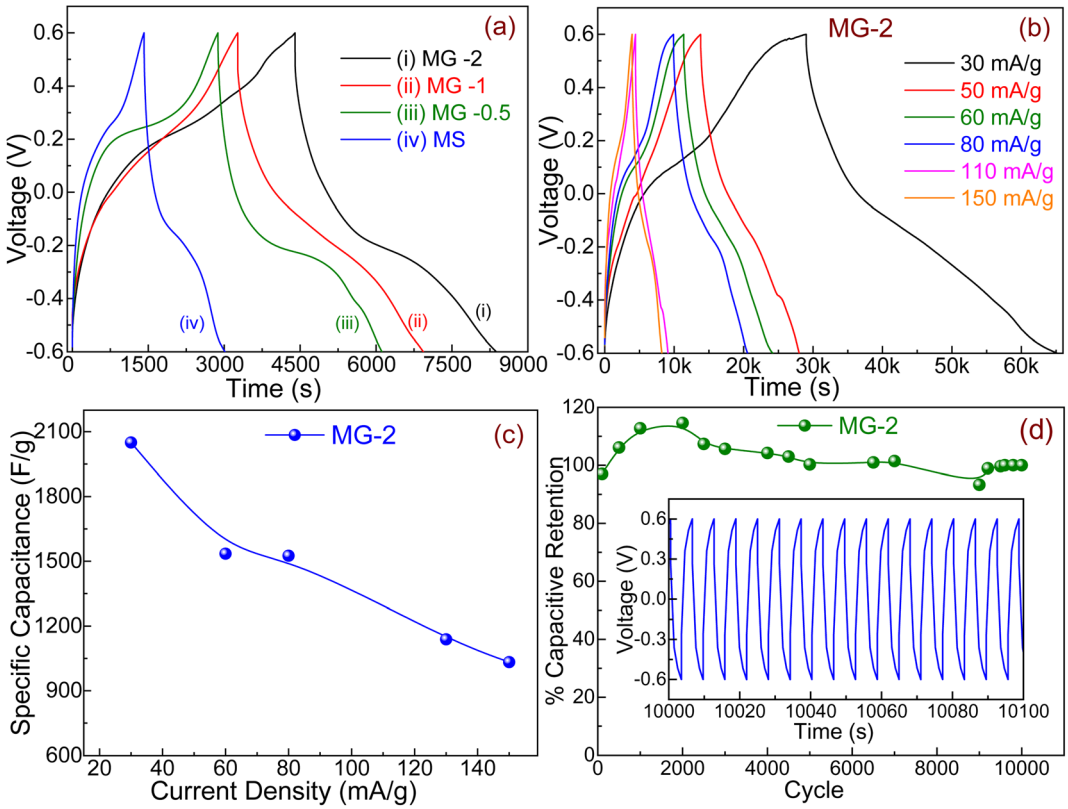

Fig. 14 (a) GCD plots of MS, MG-0.5, MG-1, and MG-2 nanohybrids at a current density of 150 mA g^{-1}; (b) GCD curves of MG-2 at varying current densities (30–150 mA g^{-1}); (c) variation in specific capacitance of MG-2 with current density; and (d) cyclic performance of MG-2 for up to 10 000 cycles, with the inset showing the GCD for a few cycles.

Table 1 Calculated C_S values of MG-2 nanohybrid using CV and GCD data

CV data		GCD data	
Scan rate (mV s^{-1})	C_S (F g^{-1})	Current density (mA g^{-1})	C_S (F g^{-1})
0.2	1397.85	30	2049.90
0.5	1364.67	60	1535.15
0.6	1284.22	80	1525.74
0.8	1247.42	130	1138.93
1	1249.68	150	1032.98
2	1122.09		
4	872.97		
5	877.19		

behaviour. The inset of Fig. 16(a) shows an expanded section of EIS data at high frequency.

Furthermore, equivalent circuit models were provided to discuss the behaviour of the supercapacitor, which were in good agreement with the experimentally observed data as reported earlier.[43,56] The inset of Fig. 16(a) elucidates the equivalent circuit models. By fitting the EIS data, the values of R_s, R_{ct}, and R_T for MG-2 nanohybrid were calculated as 2.741, 1.466, and 16.05 Ω, respectively. Considering all the nanohybrids, MG-2 exhibited the smallest charge-transfer resistance (R_{ct}). The lowest R_{ct} value for MG-2 indicated its better electrical conductivity, which was credited to the characteristics of 1T-MS. In addition, the improved charge-transfer properties of MG-2 nanohybrid were supported by the better interfacial contact between MS and rGO in the nanohybrid. A Bode plot, which depicts the fluctuation of the real or imaginary components of impedance with frequency, may also be used to deduce the supercapacitor properties.

The response frequency (f_o) is measured from the point at which both elements of the impedance become similar. The inverse of f_o is a characteristic of the response time (τ_o). These two factors have significance in determining the rate capability of a supercapacitor. Fig. 16(b) displays Bode diagrams of MG-2 nanohybrid. The value of the response frequency was measured to be 25 mHz and the corresponding response time was 40 s, demonstrating the relatively fast rate capability of the device. These findings show that the simple dip-coating method facilitated good adhesion between the electrode material and Ni foam. This might be because the van der Waals interaction between the active material and Ni foam was minimal. Furthermore, the high conductivity and porous structure of Ni foam offer a vital conductive route and bulk level exchanges for ion/electron passage for redox reactions.[38]

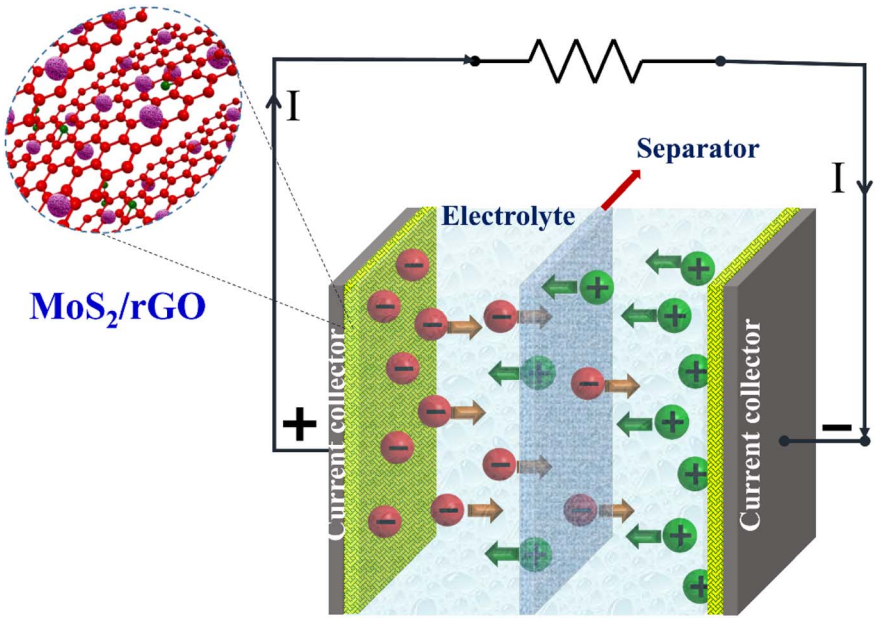

Fig. 15 Schematic design of the supercapacitor electrode assembly.

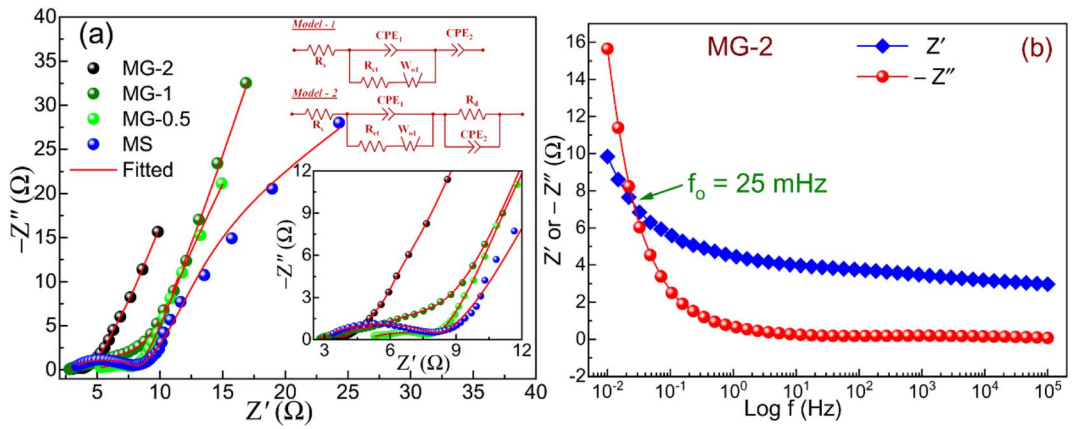

Fig. 16 (a) Nyquist plots of MS and MG nanohybrids; insets show the magnified portion of the plot in the high-frequency region and analogous equivalent circuit models. (b) Bode plots of MG-2 nanohybrid.

4. Conclusions

In summary, a one-pot facile and cost-effective strategy was adopted to synthesize MoS_2/rGO nanohybrid *via* a hydrothermal reaction. The as-synthesized nanohybrid structure featured a good distribution of 1T/2H phases, which were heavily exposed for electrolyte interaction, making them suitable for surface redox reactions. The in-depth morphological and microstructural traits of the prepared samples were confirmed using XRD, FESEM, HRTEM, EDX, and N_2 adsorption–desorption isotherms. Raman and XPS techniques were used to analyze the phase-tuned MS and MG nanohybrid structures. The findings confirmed the decoration of mixed-phase MS onto rGO nanosheets arrays, which improved the active site accessibility and electron transmission phenomena. The resultant MG-2 nanohybrid exhibited outstanding supercapacitor performance in terms of a high C_s of 2049.90 F g^{-1} at 30 mA g^{-1}, and approx. 100% capacitance retention for up to 10 000 charge–discharge cycles. Further investigation of the charge-storage mechanism using Trassati's and Dunn's methods suggested that the total capacitance was governed by the surface capacitive process. The MG-2 nanohybrid-based supercapacitor could operate within a potential window of 1.2 V and achieved $E_{s\ (max)}$ of 192.43 W h kg^{-1} at a P_s of 337.36 W kg^{-1}. Therefore, the present research work paves the way for developing innovative 2D heterostructures that will substantially improve the attributes of next-generation energy-storage technologies.

Conflicts of interest

There are no conflicts to declare.

Acknowledgements

The authors acknowledge the financial support received from the University Grants Commission, New Delhi and the Department of Science and Technology, New Delhi, under UGC-SAP {F530/5/DRS/2012(SAP-1)} and DST-FIST (SR/FST/PSI-162/2011) programs, respectively. SS is thankful to CSIR, New Delhi, for providing the necessary fellowship under 09/382(0198)/2017-EMR-I.

References

1 G. Wang, L. Zhang and J. Zhang, *Chem. Soc. Rev.*, 2012, **41**, 797–828.
2 P. Lamba, P. Singh, P. Singh, P. Singh, A. Kumar, M. Gupta and Y. Kumar, *J. Energy Storage*, 2022, **48**, 103871.
3 T. Yue, B. Shen and P. Gao, *Renew. Sustain. Energy Rev.*, 2022, **158**, 112131.
4 S. Sardana, A. Gupta, K. Singh, A. S. Maan and A. Ohlan, *J. Energy Storage*, 2022, **45**, 103510.
5 H. Xia, Q. Xu and J. Zhang, *Nano-Micro Lett.*, 2018, **10**, 1–30.
6 M. Chhowalla, H. S. Shin, G. Eda, L. J. Li, K. P. Loh and H. Zhang, *Nat. Chem.*, 2013, **5**, 263–275.
7 V. Nicolosi, M. Chhowalla, M. G. Kanatzidis, M. S. Strano and J. N. Coleman, *Science*, 2013, **340**(6139), 1226419.
8 Z. Zeng, Z. Yin, X. Huang, H. Li, Q. He, G. Lu, F. Boey and H. Zhang, *Angew. Chem.*, 2011, **123**, 11289–11293.
9 R. F. Frindt, *J. Appl. Phys.*, 1966, **37**, 1928–1929.
10 R. Barik and P. P. Ingole, *Curr. Opin. Electrochem.*, 2020, **21**, 327–334.
11 M. Israr, J. Iqbal, A. Arshad, A. Sadaf, M. Rani, M. Rani and S. Jabeen, *J. Phys. D: Appl. Phys.*, 2021, **54**(39), 395501.
12 K. S. Novoselov, V. I. Fal'Ko, L. Colombo, P. R. Gellert, M. G. Schwab and K. Kim, *Nature*, 2012, **490**, 192–200.
13 S. Korkmaz and A. Kariper, *J. Energy Storage*, 2020, **27**, 101038.
14 K. Ren, Z. Liu, T. Wei and Z. Fan, *Nano-Micro Lett.*, 2021, **13**, 1–32.
15 J. Theerthagiri, R. A. Senthil, P. Nithyadharseni, S. J. Lee, G. Durai, P. Kuppusami, J. Madhavan and M. Y. Choi, *Ceram. Int.*, 2020, **46**, 14317–14345.
16 Y. Chen, J. Bai, D. Yang, P. Sun and X. Li, *Electrochim. Acta*, 2020, **330**, 135205.
17 D. Sarmah and A. Kumar, *Electrochim. Acta*, 2019, **312**, 392–410.
18 Y. Shu, L. Zhang, H. Cai, Y. Yang, J. Zeng, D. Ma and Q. Gao, *Sens. Actuators, B*, 2020, **311**, 127863.
19 M. B. Poudel, H. P. Karki and H. J. Kim, *J. Energy Storage*, 2020, **32**, 101693.
20 M. Miah, T. K. Mondal, A. Ghosh and S. K. Saha, *Electrochim. Acta*, 2020, **354**, 136675.
21 Z. Li, X. Meng and Z. Zhang, *J. Photochem. Photobiol., C*, 2018, **35**, 39–55.
22 A.-J. Cho, M.-K. Song, D.-W. Kang and J.-Y. Kwon, *ACS Appl. Mater. Interfaces*, 2018, **10**, 35972–35977.
23 S. Zheng, L. Zheng, Z. Zhu, J. Chen, J. Kang, Z. Huang and D. Yang, *Nano-Micro Lett.*, 2018, **10**, 1–11.
24 T. Lin, T. Sadhasivam, A. Wang, T. Chen, J. Lin and L. Shao, *ChemElectroChem*, 2018, **5**, 1024–1031.
25 Y. Chao, Y. Ge, Z. Chen, X. Cui, C. Zhao, C. Wang and G. G. Wallace, *ACS Appl. Mater. Interfaces*, 2021, **13**, 7285–7296.
26 A. Gigot, M. Fontana, M. Serrapede, M. Castellino, S. Bianco, M. Armandi, B. Bonelli, C. F. Pirri, E. Tresso and P. Rivolo, *ACS Appl. Mater. Interfaces*, 2016, **8**, 32842–32852.
27 C. Zhang, J. Ning, B. Wang, H. Guo, X. Feng, X. Shen, Y. Jia, J. Dong, D. Wang and J. Zhang, *Nano Res.*, 2021, **14**, 114–121.
28 L. Jiang, S. Zhang, S. A. Kulinich, X. Song, J. Zhu, X. Wang and H. Zeng, *Mater. Res. Lett.*, 2015, **3**, 177–183.
29 H. Lv, Q. Pan, Y. Song, X.-X. Liu and T. Liu, *Nano-Micro Lett.*, 2020, **12**, 1–56.
30 L. Q. Fan, G. J. Liu, C. Y. Zhang, J. H. Wu and Y. L. Wei, *Int. J. Hydrogen Energy*, 2015, **40**, 10150–10157.
31 M. Choi, J. Hwang, H. Setiadi, W. Chang and J. Kim, *J. Supercrit. Fluids*, 2017, **127**, 81–89.
32 X. Wang, H. Feng, Y. Wu and L. Jiao, *J. Am. Chem. Soc.*, 2013, **135**, 5304–5307.
33 A. Jawaid, D. Nepal, K. Park, M. Jespersen, A. Qualley, P. Mirau, L. F. Drummy and R. A. Vaia, *Chem. Mater.*, 2016, **28**, 337–348.
34 G. S. Bang, K. W. Nam, J. Y. Kim, J. Shin, J. W. Choi and S.-Y. Choi, *ACS Appl. Mater. Interfaces*, 2014, **6**, 7084–7089.
35 S. S. Chou, M. De, J. Kim, S. Byun, C. Dykstra, J. Yu, J. Huang and V. P. Dravid, *J. Am. Chem. Soc.*, 2013, **135**, 4584–4587.
36 J. Wang, Q. Luo, C. Luo, H. Lin, R. Qi, N. Zhong and H. Peng, *J. Solid State Electrochem.*, 2017, **21**, 2071–2077.
37 S. Balendhran, J. Z. Ou, M. Bhaskaran, S. Sriram, S. Ippolito, Z. Vasic, E. Kats, S. Bhargava, S. Zhuiykov and K. Kalantar-Zadeh, *Nanoscale*, 2012, **4**, 461–466.
38 K. Krishnamoorthy, G. K. Veerasubramani, S. Radhakrishnan and S. J. Kim, *Mater. Res. Bull.*, 2014, **50**, 499–502.
39 X. Zheng, Y. Zhu, Y. Sun and Q. Jiao, *J. Power Sources*, 2018, **395**, 318–327.
40 C. Chang, X. Yang, S. Xiang, H. Que and M. Li, *J. Mater. Sci.: Mater. Electron.*, 2017, **28**, 1777–1784.
41 G. Ma, H. Peng, J. Mu, H. Huang, X. Zhou and Z. Lei, *J. Power Sources*, 2013, **229**, 72–78.
42 M. A. Bissett, I. A. Kinloch and R. A. W. Dryfe, *ACS Appl. Mater. Interfaces*, 2015, **7**, 17388–17398.
43 S. Sardana, K. Aggarwal, P. Siwach, L. Gaba, A. S. Maan, K. Singh and A. Ohlan, *Energy Storage*, 2022, e328.
44 M. M. Baig, E. Pervaiz, M. Yang and I. H. Gul, *Front. Mater.*, 2020, **7**, 323.
45 M. Wu, J. Zhan, K. Wu, Z. Li, L. Wang, B. Geng, L. Wang and D. Pan, *J. Mater. Chem. A*, 2017, **5**, 14061–14069.
46 K.-J. Huang, J.-Z. Zhang, G.-W. Shi and Y.-M. Liu, *Electrochim. Acta*, 2014, **132**, 397–403.
47 P. V Shinde, N. M. Shinde, J. M. Yun, R. S. Mane and K. H. Kim, *ACS Omega*, 2019, **4**, 11093–11102.
48 H. Sun, H. Liu, Z. Hou, R. Zhou, X. Liu and J.-G. Wang, *Chem. Eng. J.*, 2020, **387**, 124204.
49 J. Shao, X. Zhou, Q. Liu, R. Zou, W. Li, J. Yang and J. Hu, *J. Mater. Chem. A*, 2015, **3**, 6168–6176.

50 V. Šedajová, P. Jakubec, A. Bakandritsos, V. Ranc and M. Otyepka, *Nanomaterials*, 2020, **10**, 1731.
51 J. Wang, J. Polleux, J. Lim and B. Dunn, *J. Phys. Chem. C*, 2007, **111**, 14925–14931.
52 C.-W. Lien, B. Vedhanarayanan, J.-H. Chen, J.-Y. Lin, H.-H. Tsai, L.-D. Shao and T.-W. Lin, *Chem. Eng. J.*, 2021, **405**, 126706.
53 Z. Jiang, Y. Wang, S. Yuan, L. Shi, N. Wang, J. Xiong, W. Lai, X. Wang, F. Kang and W. Lin, *Adv. Funct. Mater.*, 2019, **29**, 1807116.
54 N. Choudhary, C. Li, H.-S. Chung, J. Moore, J. Thomas and Y. Jung, *ACS Nano*, 2016, **10**, 10726–10735.
55 S. Sardana, A. Gupta, A. S. Maan, S. Dahiya, K. Singh and A. Ohlan, *Indian J. Phys.*, 2022, **96**, 433–439.
56 A. Gupta, S. Sardana, J. Dalal, S. Lather, A. S. Maan, R. Tripathi, R. Punia, K. Singh and A. Ohlan, *ACS Appl. Energy Mater.*, 2020, **3**, 6434–6446.